minerals

MDPI

Article

Three-Dimensional Forward Modeling for SOTEM from Frequency-Domain Model Reduction

Saimin Zhang [1], Ken Chen [2], Jifeng Zhang [2,*], Jiren Liu [3] and Xiran You [2]

[1] College of Geophysics, Chengdu University of Technology, Chendu 610059, China; saiminzhang@126.com
[2] School of Geological Engineering and Geomatics, Chang'an University, Xi'an 710061, China; liunian2532@163.com (K.C.)
[3] School of Computer Science and Engineering, Hunan University of Science and Technology, Xiangtan 411201, China
* Correspondence: zjf0201@126.com

Abstract

The short-offset transient electromagnetic method (SOTEM) has become a popular research topic in recent years. In this paper, we present the vector finite element method based on model reduction, which greatly improves computational efficiency. Based on the Krylov subspace projection method, the electromagnetic response of multi-frequency is quickly obtained using model reduction, and the acceleration ratio reaches 33. The electromagnetic field in the time domain is obtained using cosine transformation. A translation algorithm is used to calculate the full-time apparent resistivity. The correctness of the algorithm is verified using uniform half-space model and a complex geoelectric model. Then the amplitude of the transient electromagnetic apparent resistivity anomaly of the 1D, 2D, and 3D geoelectric models is compared. Results show that the electromagnetic response amplitude from the 1D model is much greater than the ones from the 2D and 3D models. Special attention needs to be paid to the processing and interpreting field data using the 1D forward and inversion method. Additionally, we analyze the impulse responses at the different offsets for the conductive body, and the results indicate that with the decrease in the offset, the impulse response and anomalous amplitude are greatly enhanced, and exploration depth and resolution are also improved. The porphyry Cu-Mo deposit model experiment further demonstrates that three-dimensional SOTEM forward modeling combined with full-time apparent resistivity imaging can effectively identify low-resistivity mineralized anomalies within a complex geological model at depths of approximately 200–500 m, thereby confirming the applicability of the method to realistic mineral deposit exploration.

Keywords: SOTEM; LOTEM; vector finite element; model reduction; full-time apparent resistivity

Check for updates

Academic Editor: Stanisław Mazur

Received: 16 June 2026
Revised: 27 July 2026
Accepted: 27 July 2026
Published: 30 July 2026

Copyright: © 2026 by the authors. Licensee MDPI, Basel, Switzerland. This article is an open access article distributed under the terms and conditions of the Creative Commons Attribution (CC BY) license.

1. Introduction

Grounded-source transient electromagnetics method has been widely used in oil and gas resources and in geothermal and coalfield geological fields [1–3] in recent years because of its simple layout and large detection depth. Early grounded-source transient electromagnetics mainly refers to long offset transient electromagnetics (LOTEM) [4], which means that the transceiver distance is more than 4–6 times the detection depth [5]. The observation area of this method is limited, and the signal intensity decreases sharply with an increase of the transceiver distance, which affects the detection depth; moreover, multiple tectonic units between the transceiver distance maybe cause electrical changes, which is not conducive to fine detection, so LOTEM is mostly used in areas with simple

structure and flat terrain [6–8]. As the detection accuracy and depth requirements become higher and higher, the short-offset method has been proposed and has become a research focus [9]. The short-offset method is easy to apply in complex terrain exploration because the transceiver distance is less than or equal to the detection depth and the signal strength increases, which is obviously better than the transient electromagnetics of the loop source.

The short-offset transient electromagnetic method (SOTEM) has attracted increasing attention as a near-source electromagnetic exploration technique because of its strong signal intensity, broad effective bandwidth, and potential for high-resolution deep exploration [1,7,10–12]. Previous studies have mainly focused on one-dimensional forward modeling and inversion, response characteristics, data processing, and engineering applications in mineral exploration, coalfield hydrogeology, and structural investigation [7,13–15]. Although several studies have recently addressed three-dimensional forward modeling, source effects, imaging, and inversion [16–18], systematic investigations of three-dimensional SOTEM responses remain relatively limited.

The 3D electromagnetic response analysis method is mainly based on numerical simulation methods, as follows: the finite difference method [19], the integral equation method [20–22], the finite element method [23–25], etc. The finite element method has been widely used in geophysical electromagnetic modeling in recent years due to its flexible mesh generation. Due to the discontinuity of normal components of an electric field, node-based finite element methods often cause the spurious solution phenomenon [26,27]. There are three main methods to overcome the spurious solution phenomenon. One way is to force the electric field divergence to zero by applying the divergence condition; the second way is to adopt the node finite element method based on vector-scalar potential [28,29]. The vector finite element changes the shape function; automatically satisfies the electromagnetic field divergence condition in each the element, without applying any conditions; and is widely used in geophysical electromagnetic simulations [30–32].

At present, there are two main approaches for obtaining three-dimensional transient electromagnetic responses. One is to calculate the electromagnetic response directly in the time domain; the other is to calculate the electromagnetic fields at multiple frequency points in the frequency domain and then obtain the corresponding time-domain responses using sine or cosine transforms [31,33–36]. The latter method is relatively simple and can directly utilize the numerical results of the frequency domain. But to achieve high accuracy, it usually takes dozens or even hundreds of frequencies to complete the calculation, and it is very time-consuming to solve a large sparse linear equation for each frequency [36–38]. Fortunately, based on the Krylov subspace projection method, the model reduction method fundamentally overcomes this shortcoming [33,39,40]. Consequently, the number of frequency points is no longer the dominant factor limiting computational efficiency. Compared with the PARDISO direct solver, the model reduction method can improve the computational speed by more than one order of magnitude. This substantial acceleration makes efficient three-dimensional time-domain electromagnetic finite-element modeling feasible [41,42].

The SOTEM method has been increasingly applied to complex mineral resource exploration, particularly in areas characterized by thick cover, highly conductive overburden, and deeply concealed ore bodies. Chen et al. applied SOTEM to the exploration of deep banded iron formation BIF iron deposits beneath thick and conductive Quaternary sediments, demonstrating that the method maintains strong penetration capability in highly conductive covered areas and can effectively delineate concealed ore bodies at depths exceeding 1000 m [10]. Hou et al. further employed the E_x component of SOTEM to identify deep magnetite deposits beneath thick low-resistivity cover, and improved the positioning accuracy of magnetite bodies in complex covered areas through joint inversion of the E_x and

H_z components [43]. To address the limited efficiency and resolution of three-dimensional inversion of SOTEM data, Xue et al. proposed a particle swarm optimization–quasi-Newton PSO-QN hybrid algorithm, enabling fast and high-resolution 3D inversion of SOTEM data and providing an effective inversion tool for fine-scale mineral exploration under complex geological conditions [44]. In addition, Xue et al. applied SOTEM to the deep exploration of the Zhou'an Ni-Cu-PGE deposit and obtained high-resolution electrical structure imaging to a depth of approximately 2.5 km, further confirming the significant potential of SOTEM for deep mineral exploration. However, most existing studies have focused primarily on field verification and inversion applications, whereas systematic investigations of 3D electromagnetic response characteristics, anomaly formation mechanisms, and the influence of different acquisition parameters under complex ore-body model conditions remain relatively limited [12].

Therefore, although SOTEM has demonstrated considerable potential for deep mineral exploration, further 3D forward modeling and electromagnetic response analysis are required to clarify its response characteristics in complex geoelectric environments. In this paper, SOTEM is simulated using the vector finite element method, the frequency domain model reduction algorithm is constructed, and the time domain electromagnetic field is obtained using cosine transform. The electromagnetic response of 1D, 2D, and 3D geoelectric models is analyzed, the abnormal response and the total apparent resistivity characteristics under different offset distances are given, and the influence of different offsets on the secondary field and abnormal amplitude is analyzed.

2. Theory

SOTEM is similar to LOTEM, and the layout of SOTEM is similar to the LOTEM and CSAMT methods, see Figure 1, but the offset is generally less than two times equal to the maximum detection depth. In this range, the signal intensity is large, the abnormal response of the target body is strong, and SOTEM has more deep detection ability. At present, the main observations are the vertical induced voltage and the horizontal electric field along the direction of the source. These two components are sensitive to formation and have certain characteristics. The best detection effect can be achieved by reasonably setting the transceiver distance and selecting the observation area.

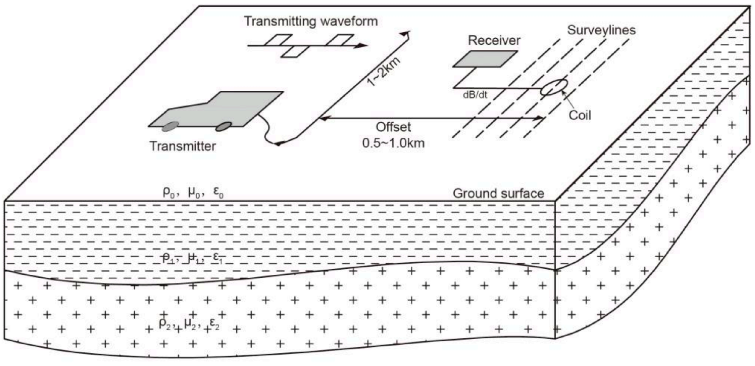


Figure 1. Schematic diagram of the SOTEM system.

3. Finite Element Analysis

3.1. Controlled Equations

In the three-dimensional electromagnetic forward modeling, the frequency domain equation under the quasi-static condition (neglecting the influence of displacement current) meets the following requirements [27]:

$$\nabla \times \mathbf{E} = -i\omega\mu_0\mathbf{H} \quad (1)$$

$$\nabla \times \mathbf{H} = \mathbf{J}_s + \sigma \mathbf{E} \tag{2}$$

The formula is based on the harmonic factor $e^{i\omega t}$, ω is the circular frequency, σ is the conductivity, μ_0 is the vacuum permeability, and J_s is an impressed electrical current density. Taking the curl of both sides of (1) and substituting (2) into the resulting equation eliminates the magnetic field **H**, yielding the following double-curl equation solely in terms of the electric field **E** as follows [27]:

$$\begin{cases} \nabla \times \nabla \times \mathbf{E} + k^2 \mathbf{E} = -i\omega\mu_0 \mathbf{J}_s \\ \mathbf{n} \times \mathbf{E} = 0 \quad on \boldsymbol{\Gamma} \end{cases} \tag{3}$$

where k is the wave number under the quasi-static limit, $k^2 = i\omega\mu_0\sigma$.

In order to solve the objective equation of (3), the electric field $\boldsymbol{E}(x, y, z; \omega)$ and the magnetic field $\mathbf{H}(x, y, z; \omega)$ corresponding to the frequency set are expected to be solved in the frequency domain, and then the electric field $\mathbf{E}(x, y, z, t)$ or the EMF (Induced electromotive force) $\zeta = \mu_0 \frac{dh(x,y,z;t)}{dt}$ in the time domain are solved by the inverse Fourier transform. In this paper, the generalized variational principle is used to obtain the variational equation of (3) [27]. For the entire computational domain Ω, the functional given in Equation (3) attains its minimum at the electric field E as follows [26,45], the complete derivation is seen the Appendix A:

$$F[\mathbf{E}] = \frac{1}{2}\int_{\Omega} [(\nabla \times \mathbf{E}) \cdot (\nabla \times \mathbf{E}) + k^2 \mathbf{E} \cdot \mathbf{E}] dV + i\omega\mu \int_{\Omega} (\mathbf{E} \cdot \mathbf{J}_s) dV \tag{4}$$

3.2. Finite Element Discretization and Model Reduction

When we use a nodal finite element to solve the variational problem, the divergence condition will not be satisfied, and a spurious solution will be generated. A better way is to add a penalty term to the equation to force it to meet the divergence condition [46]. Another even better solution is to use the vector finite element method to assign the degree of freedom directly to the edge of the element, which automatically meets the divergence condition. In this paper, a rectangular hexahedral element is used. For each element, the degrees of freedom of the vector basis functions are assigned to its 12 edges, as shown in Figure 2. The field value at any point within the element can be expressed as follows [45]:

$$E_x^e = \sum_{i=1}^{4} N_{xi}^e E_{xi}^e, E_y^e = \sum_{i=1}^{4} N_{yi}^e E_{yi}^e, E_z^e = \sum_{i=1}^{4} N_{zi}^e E_{zi}^e \tag{5}$$

where $N_{pi}^e (p = x, y, z; i = 1, ..., 4)$ is the vector basis function, and the specific expression of the vector basis function is given in the reference [27]. Using the Galerkin or Ritz method to solve the variational equation of (4), we obtain the matrix equation using each discrete element as follows [45]:

$$\sum (\mathbf{C}_e + i\omega\, \mathbf{M}_e) \cdot \mathbf{E}_e = \sum -i\omega\, \mathbf{b}_e \tag{6}$$

$$\mathbf{C}_e = \begin{bmatrix} \mathbf{C}_{xx}^e & \mathbf{C}_{xy}^e & \mathbf{C}_{xz}^e \\ \mathbf{C}_{yx}^e & \mathbf{C}_{yy}^e & \mathbf{C}_{yz}^e \\ \mathbf{C}_{zx}^e & \mathbf{C}_{zy}^e & \mathbf{C}_{zz}^e \end{bmatrix}; \mathbf{M}_e = \begin{bmatrix} \mathbf{M}_{xx}^e & 0 & 0 \\ 0 & \mathbf{M}_{yy}^e & 0 \\ 0 & 0 & \mathbf{M}_{zz}^e \end{bmatrix}; \mathbf{E}_e = \begin{bmatrix} \mathbf{E}_x^e \\ \mathbf{E}_y^e \\ \mathbf{E}_z^e \end{bmatrix};$$

$$\mathbf{E}_p^e = [E_{p1}^e, ..., E_{p4}^e]^T, (p = x, y, z);$$

$$[\mathbf{C}_{xx}^e] = \int_{\Omega^e} [(\frac{\partial\{\mathbf{N}_x^e\}}{\partial y}) \cdot (\frac{\partial\{\mathbf{N}_x^e\}}{\partial y})^T + (\frac{\partial\{\mathbf{N}_x^e\}}{\partial z}) \cdot (\frac{\partial\{\mathbf{N}_x^e\}}{\partial z})^T] dV;$$

$$\left[\mathbf{C}_{yy}^{e}\right]=\int_{\Omega^e}[(\frac{\partial\left\{\mathbf{N}_{y}^{e}\right\}}{\partial z})\cdot(\frac{\partial\left\{\mathbf{N}_{y}^{e}\right\}}{\partial z})^{T}+(\frac{\partial\left\{\mathbf{N}_{y}^{e}\right\}}{\partial x})\cdot(\frac{\partial\left\{\mathbf{N}_{y}^{e}\right\}}{\partial x})^{T}]dV;$$

$$[\mathbf{C}_{zz}^{e}]=\int_{\Omega^e}[(\frac{\partial\{\mathbf{N}_{z}^{e}\}}{\partial y})\cdot(\frac{\partial\{\mathbf{N}_{z}^{e}\}}{\partial y})^{T}+(\frac{\partial\{\mathbf{N}_{z}^{e}\}}{\partial x})\cdot(\frac{\partial\{\mathbf{N}_{z}^{e}\}}{\partial x})^{T}]dV;$$

$$\left[\mathbf{C}_{xy}^{e}\right]=-\int_{\Omega^e}(\frac{\partial\{\mathbf{N}_{x}^{e}\}}{\partial y})\cdot(\frac{\partial\left\{\mathbf{N}_{y}^{e}\right\}}{\partial x})^{T}\,dV;$$

$$[\mathbf{C}_{zx}^{e}]=-\int_{\Omega^e}(\frac{\partial\{\mathbf{N}_{x}^{e}\}}{\partial z})\cdot(\frac{\partial\{\mathbf{N}_{z}^{e}\}}{\partial x})^{T}dV;$$

$$\left[\mathbf{C}_{yz}^{e}\right]=-\int_{\Omega^e}(\frac{\partial\left\{\mathbf{N}_{y}^{e}\right\}}{\partial z})\cdot(\frac{\partial\{\mathbf{N}_{z}^{e}\}}{\partial y})^{T}dV;$$

$$\mathbf{C}_{yx}=\mathbf{C}_{xy}^{\mathbf{T}};\mathbf{C}_{yz}=\mathbf{C}_{zy}^{\mathbf{T}};\mathbf{C}_{zx}=\mathbf{C}_{xz}^{\mathbf{T}};$$

$$\left[\mathbf{M}_{pp}^{e}\right]=\mu\sigma\int_{\Omega^e}\left\{\mathbf{N}_{p}^{e}\right\}\cdot\left\{\mathbf{N}_{p}^{e}\right\}^{T}dV,(p,q=x,y,z);$$

The right term $[\mathbf{b}_e]=\begin{bmatrix}\mathbf{b}_x^e\\ \mathbf{b}_y^e\\ \mathbf{b}_z^e\end{bmatrix}$ of the equation is related to the supply direction of the electric source. If the electric source deviates from the electric dipole, it should be treated in sections. Where $\mathbf{b}_p^e=\mu\int_{\Omega^e}\left\{\mathbf{N}_p^e\right\}\cdot\mathbf{J}_e dV,(p=x,y,z)$, for the long wire source, we directly load each segment of the source on the edge of the grid according to its intersection segment with the grid unit. For the current source distributed in an element e, we can get $\left[\mathbf{b}_p^e\right]=IdL\cdot\mu\left\{N_p^e(x_0,y_0,z_0)\right\},(p=x,y,z)$, where IdL is the electric dipole moment of the segment, and (x_0,y_0,z_0) is the midpoint coordinate of the segment.

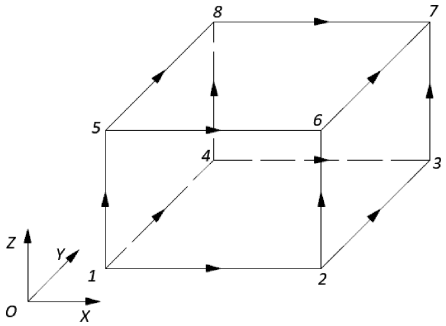


Figure 2. Rectangular hexahedral element (the number refers to node and arrow refers to degree of freedom).

By assembling the element equations over all edges, Equation (6) can be expressed in the following global matrix form and its equivalent form [45]:

$$(\mathbf{C}+i\omega\mathbf{M})\cdot\mathbf{E}=-i\omega\,\mathbf{b} \tag{7}$$

$$(\mathbf{M}^{-1}\mathbf{C}+i\omega\,\mathbf{I})\cdot\mathbf{E}=-i\omega\mathbf{M}^{-1}\mathbf{b} \tag{8}$$

To reconstruct the time-domain response through an inverse Fourier transform, the frequency-domain electromagnetic fields must be evaluated over an appropriately sampled frequency range. In the conventional direct-solution approach, a large sparse linear system must be solved independently at each sampled frequency. Therefore, the repeated solution of these systems results in considerable computational cost. In this paper, the model reduction algorithm of monopole is used to simplify the operation system. It only needs to solve the equation once, and multiple matrix substitutions can quickly obtain the response of multiple frequency points, which greatly improves operation efficiency [33].

The model reduction algorithm is an approximate operation which can obtain the approximate value of the direct solution under higher accuracy. Here, we use the direct solution (9) and the calculation expression after model reduction (10), as follows [40,47]:

$$\mathbf{E} = -i\omega(\mathbf{A} + i\omega\,\mathbf{I})^{-1}\mathbf{X} = g^{\omega}(\mathbf{A})\mathbf{X} \tag{9}$$

$$\mathbf{E} = ||\mathbf{b}||_M \mathbf{V}_{m+1} g^{\omega}(\mathbf{A}_{m+1})\mathbf{e}_1 \tag{10}$$

where $\mathbf{A} = \mathbf{M^{-1}C}, \mathbf{X} = \mathbf{M^{-1}b}$, we call $g^{\omega}(\mathbf{A})$ the transfer function [48] and $\mathbf{e}_1 = [1,0,0,\ldots]^T \in \mathbf{R^{m+1}}$, $\mathbf{A}_{m+1} = \mathbf{V}_{m+1}^T\mathbf{M}\mathbf{A}\mathbf{V}_{m+1} = \mathbf{V}_{m+1}^T\mathbf{C}\mathbf{V}_{m+1}$. $\mathbf{A}_{m+1}$ is the orthogonal projection of $\mathbf{A}$ to $\mathbf{V}_{m+1}$, and the dimension is far smaller than matrix A. $\mathbf{V}_{m+1}$ is the standard column orthogonal vector calculated by the variant of Arnoldi algorithm. See the reference for the detailed model reduction process [31,40]. Zhou et al. [40] proposed that a single repeated pole $\xi_0 = -2\pi\sqrt{f_{\min}f_{\max}} < 0$ can be used to reduce the order of the model. Only one matrix solution is needed, and the matrix back m times substitution can quickly obtain the order reduction solution of the model with multiple frequency points.

3.3. Calculation of Magnetic Field and Inverse Fourier Transform

Through the model reduction algorithm for fast multi- frequency, the electric field of each grid cell edge can be obtained, and the corresponding magnetic field can be calculated through (1). The research objective of this paper is the EMF, so we need to get the value of the vertical component Hz of the magnetic field at any point, as follows [45]:

$$H_z = \frac{1}{i\omega\mu}\left(\frac{\partial E_x}{\partial y} - \frac{\partial E_y}{\partial x}\right) \tag{11}$$

The derivative of the electric field can be obtained from the corresponding vector basis function, as follows [45]:

$$\frac{\partial E_p}{\partial q} = \sum_{i=1}^{4}\frac{\partial N_p}{\partial q}E_{pi}, (p,q = x,y,z) \tag{12}$$

In order to obtain the time domain transient electromagnetic response $h_z(t)$ on the ground, we can use the response obtained in the frequency domain, then we use the inverse Fourier transform to obtain its integral expression, and finally we use the real part and the virtual part to calculate the time domain response, respectively, as follows [49]:

$$h_z(t) = \frac{1}{2\pi}\int_{-\infty}^{+\infty}\frac{H_Z(\omega)}{-i\omega}e^{-i\omega t}d\omega \tag{13}$$

$$h_z(t) = \frac{2}{\pi}\int_{0}^{+\infty}\mathrm{Re}(H_z(\omega))\frac{\sin\omega t}{\omega}d\omega = \frac{2}{\pi}\int_{0}^{+\infty}\mathrm{Im}(H_z(\omega)\frac{\cos\omega t}{\omega}d\omega \tag{14}$$

As for the EMF, we only need to use the derivative property of Fourier transform to obtain [49], as follows:

$$\zeta = \mu_0 \frac{\mathrm{d}h_z(t)}{dt} = -\frac{2}{\pi}\int_0^{+\infty} \mathrm{Re}(H_z(\omega))\cos(\omega t)d\omega = -\frac{2}{\pi}\int_0^{+\infty} \mathrm{Im}(H_z(\omega))\sin(\omega t)d\omega \quad (15)$$

For the above integral, we usually use the Fast Hankel transform to solve it.

3.4. Full-Time Apparent Resistivity Calculation

For the transient electromagnetic method of long electrical sources, the calculation formula of apparent resistivity in the early or late time of the limit case is usually used, which brings great inconvenience, not only because two methods are used to calculate the apparent resistivity in the early "absolute" and the late "absolute" stage, respectively, but also because the information of most of the middle section is lost, resulting in the distortion of the apparent resistivity curve. This seriously affects the detection ability of TEM. We can follow the wide-field electromagnetic method in the frequency domain [50] and introduce full-time apparent resistivity for all sampling time channels. We introduce the calculation method of full-time apparent resistivity based on the EMF force generated by the vertical magnetic field of the electrical source.

The expression of the EMF of the transient electromagnetic field generated by the step current emitted by the dipole source on the surface of the uniform half-space is as follows [49]:

$$\zeta = \mu_0 \frac{\mathrm{d}h_z(t)}{dt} = -\frac{3IdL\rho}{2\pi r^4}\sin\varphi\left[\Phi(u) - \sqrt{\frac{2}{\pi}}u(1+u^2/3)e^{-u^2/2}\right] \quad (16)$$

where IdL is the electric dipole moment, φ is the angle between the line of from the measuring point to the center of the electric dipole and the electric dipole, u is the induction number ($u = 2\pi r/\tau, \tau = 2\pi\sqrt{2\rho t/\mu_0}$), and $\Phi(u) = \sqrt{\frac{2}{\pi}}\int_0^u e^{-x^2/2}dx$ is the probability integral. If we can device the expression of resistivity from Equation (16), we can obtain the apparent resistivity of full-time windows, which can reflect the electrical properties of underground media. Equation (16) is an implicit function of resistivity. We can get full-time apparent resistivity by iteration or dichotomy using the 1D forward program.

In order to reduce the errors introduced by the iterative algorithm and enhance the applicability of the program for 3D numerical simulation, we introduce the translation algorithm of full-time apparent resistivity. We found that the transient electromagnetic EMF response curve of the electrical source has the characteristics of translation and expansion, which is similar to the EMF curve of the central loop [51]. That is to say, the transient electromagnetic response curve of the homogeneous half-space model with resistivity of $K\rho$ at a certain measuring point can be obtained by translating the transient electromagnetic response curve of the homogeneous half-space with resistivity of ρ at the same measurement point, as shown in Figure 3a.

Figure 3b shows the schematic diagram of the translation algorithm. For any given ρ_0, the theoretical translation intercept of the time trace t_i is [51], as follows:

$$B_0(t_i) = \log(t_i) + \log\varepsilon_z(\rho_0, t_i) \quad (17)$$

When the sampling delay corresponding to the input EMF is t_j, the translation intercept is as follows:

$$B_s(t_j) = \log(t_j) + \log(\varepsilon_z)_j \quad (18)$$

If $B_s(t_j) = B_0(t_i)$, the full-time apparent resistivity of the input data at time t_j is as follows [51]:

$$\rho_{sj} = \frac{t_i}{t_j}\rho_0 \tag{19}$$

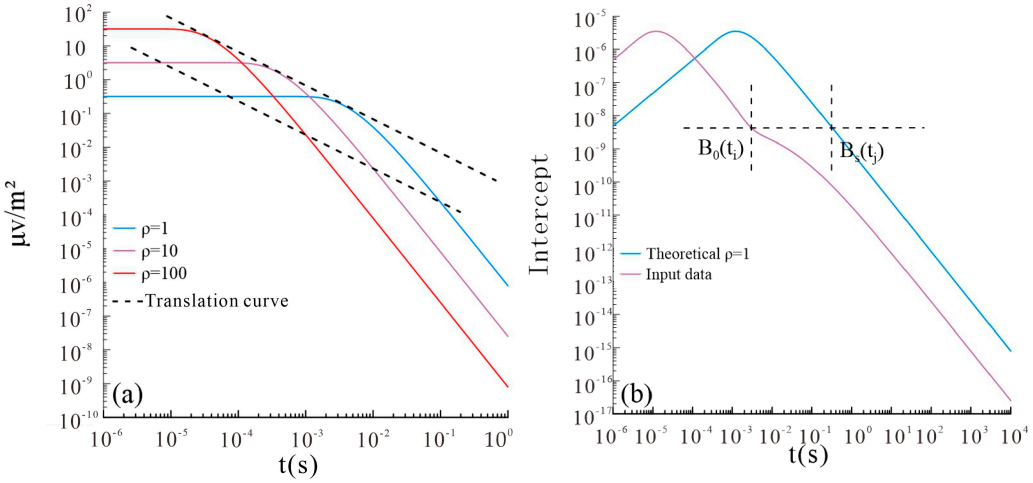


Figure 3. Schematic chart of translation characteristic and algorithm of db/dt for electrical source: (**a**) Translation characteristic, (**b**) Translation algorithm.

4. Numerical Example

The program can be run on any computer installed with windows10 or above. It requires two software, as follows: the visual studio 2013 and Intel visual FORTRAN 2013 version or above. The program language is Fortran90, and the size of program is 92 KB. For the largest model considered in this study, the memory required to store the sparse coefficient matrix and the principal solution arrays was approximately 0.96 GB.

4.1. Correction Inspection of Procedures

In order to test the correctness of the algorithm, we first establish a uniform half-space model of resistivity at 100 Ω·m. The direction of electric dipole is along the x-axis, the electric dipole moment IdL is 1000 Am, and the measuring point location is (−1200 m, −1200 m, 0 m).

In the verification test, the transient responses were calculated using 31 logarithmically spaced time channels ranging from 10^{-5} s to 10^{-2} s. The time sampling interval was defined as follows:

$$t_i = 10^{-5} \times 10^{i/10},\ i = 0, 1, \ldots, 30$$

Considering the effective response range and computational efficiency, the first 25 time channels were selected for analysis. The frequency-domain electromagnetic responses were calculated at the specified sampling frequencies and then transformed into the time-domain responses using an inverse Fourier transform. The frequency sampling was determined according to the following:

$$f_k = \frac{\exp(k\Delta)}{2\pi t}$$

with $\Delta = 10^{-3}$. The frequency index k varied from −149 to 100, resulting in 250 frequency sampling points. Based on the selected time range, the corresponding frequency range was from 54.6 Hz to 1.76×10^4 Hz.

To quantitatively evaluate the agreement between the proposed algorithm and the reference solution, the relative error was defined as follows:

$$\varepsilon_i = \frac{\left|X_i^{cal} - X_i^{ref}\right|}{\left|X_i^{ref}\right|} \times 100\%$$

where X_i^{cal} and X_i^{ref} represent the calculated results obtained by the proposed algorithm and the reference solution at the *i*-th time channel, respectively.

In Figure 4a, we can see that EMF and full-time apparent resistivity are in good agreement, and the maximum error is less than 3%. Figure 4b shows that full-time apparent resistivity tends to the true resistivity using the translation algorithm.

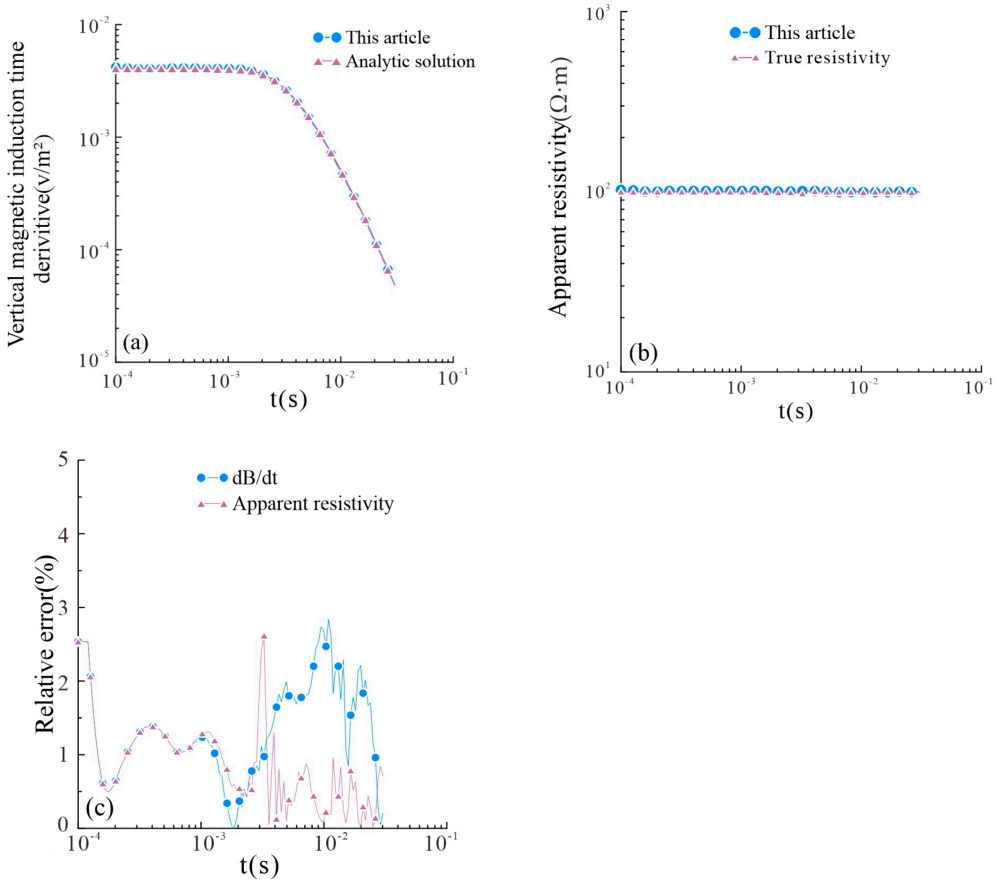


Figure 4. Comparison of the homogeneous half-space numerical solution obtained in this article with the one-dimensional analytical solution: (**a**) db/dt, (**b**) full-time apparent resistivity, (**c**) relative error.

In order to verify the efficiency of the model reduction algorithm in the SOTEM numerical modeling, we compare the calculation time of model reduction algorithm with that of the 3D finite element direct solution (3DFEM). The calculation speed of the model reduction method is much higher than that of the 3DFEM; the solution time of 3DFEM is 6666 s, while that of model reduction is 202 s, as Table 1 shows. The acceleration ratio reaches 33; the more frequencies there are, the larger the acceleration ratio is, which greatly improves the computational efficiency from frequency domain to time domain.

In order to test the applicability of the 3D model, we compare the results with the mimicry finite volume method (MFVRK) of Liu et al. [52]. First, we established the model as shown in Figure 5 [53], and placed a 100 m long electrical source along the y-direction, with the midpoint of the electrical source at the origin, and set three receiving points at x = 200 m, x = 400 m, x = 1000 m. The first layer is a thin layer with a resistivity of 10 Ω·m and a

thickness of 50 m. A vertical contact surface is set at x = 400 m, with a resistivity of 100 Ω·m and 300 Ω·m on both sides, respectively. There is a complex low-resistance body placed at the vertical contact surface, the top depth is 50 m, the bottom depth is 550 m, the strike extension 400 m, and the resistivity is 1 Ω·m. Figure 6 is the comparison curve between the algorithm in this paper and the solution of Liu et al. [52]. The EMF changes with time at three measuring points are described. It can be seen that the solutions of the two algorithms agree well, which verifies the feasibility of this algorithm in 3D model forward problem.

Table 1. Comparison of calculation time.

	Number of Nodes	Number of Elements	Number of Frequencies	Number of Freedom	Time/s
3DFEM	198,528	188,370	60	595,584	6666
Model reduction	198,528	188,370	60	595,584	202

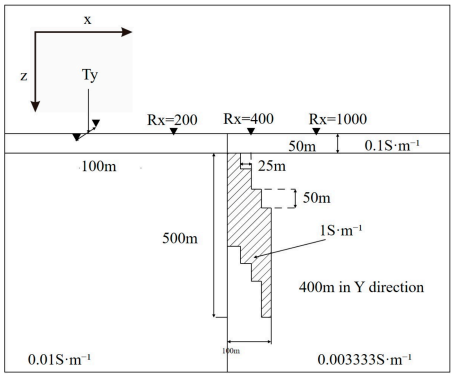


Figure 5. Model diagram.

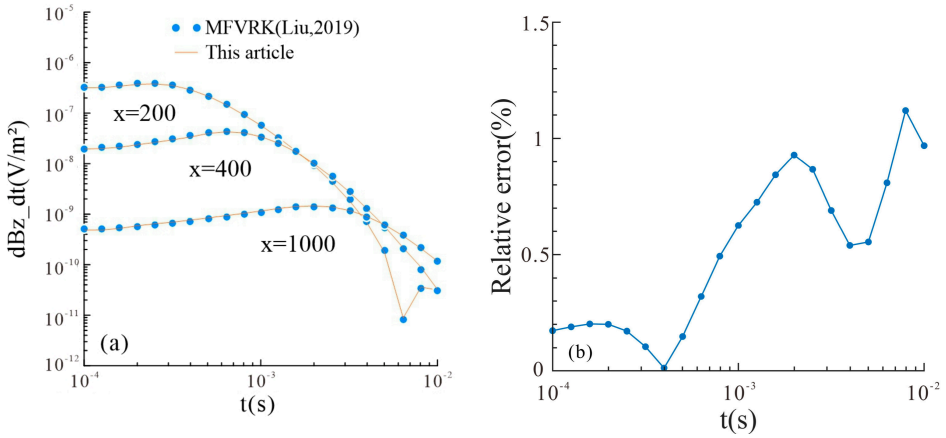


Figure 6. The comparison between the numerical solution in this article and the MFVRK numerical solution: (**a**) db/dt, (**b**) relative difference [52].

4.2. Comparison of 1D, 2D, and 3D Models

In the processing interpretation of field data, due to the complexity of the calculation, we often use a one-dimensional or two-dimensional transient electromagnetic model. However, strictly speaking, all geoelectric models are three-dimensional ones. To achieve good exploration results, only transient electromagnetic responses are analyzed from a three-dimensional full-space perspective. Next, we briefly discuss the difference between the transient electromagnetic response of a three-dimensional geological body and 1D and 2D. First, we establish the model as follows: the size of the anomalous

body is 400 m × 400 m × 400 m, the central coordinate of the abnormal body is (−1200 m, −1200 m, 400 m), the resistivity of the abnormal body is 5 Ω·m, and the resistivity of the surrounding rock is 100 Ω·m, as shown in Figure 7. We place a 100 m long electrical source on the x-axis, and the midpoint coordinate of the source is (0 m, 0 m, 0 m). Meanwhile, when the anomalous body extends infinitely in the y-direction while retaining a finite extent in the x-direction, it represents a two-dimensional model. When it extends infinitely in both the x- and y-directions, it represents a one-dimensional horizontally layered model. Figure 8 shows the full-time apparent resistivity curves derived from the transient electromagnetic responses of the three models. The results demonstrate that the apparent resistivity responses obtained from the 3D geoelectric model are slightly different from those of the 2D model, while both exhibit much weaker anomaly contrasts compared with the 1D geological model. This difference is attributed to the dimensional effects of the geoelectric structures on the transient electromagnetic responses and their subsequent apparent-resistivity transformation.

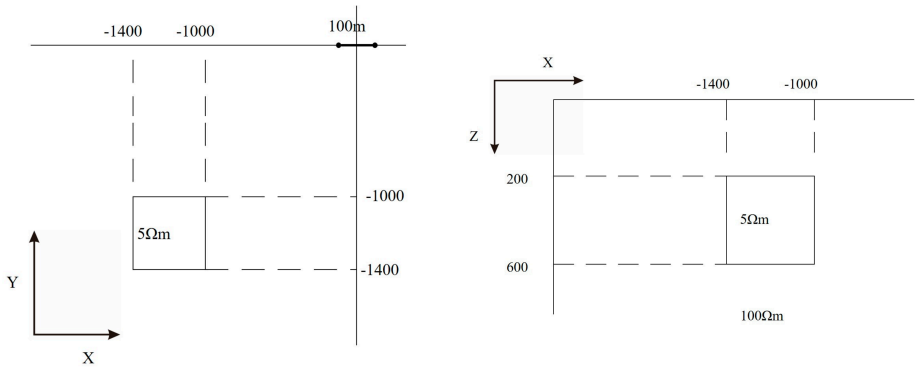


Figure 7. Single cube anomaly model diagram: (**a**) XOY-section, (**b**) XOZ-section.

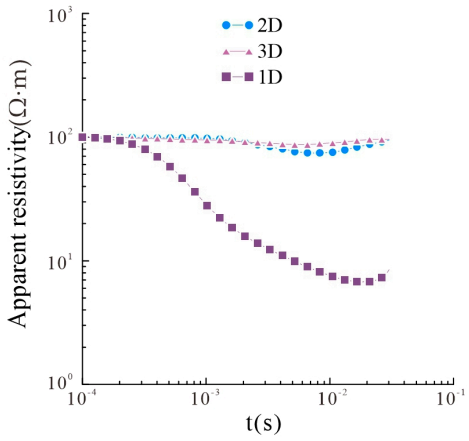


Figure 8. Comparison of full-time apparent resistivity responses obtained from the 1D, 2D, and 3D models.

Because the apparent resistivity is an equivalent parameter calculated from the transient electromagnetic response based on a reference earth model, it does not directly represent the true resistivity distribution of the subsurface. The responses of finite-size 2D and 3D geological bodies are affected by lateral current flow and finite geometric boundaries, resulting in reduced apparent-resistivity anomalies compared with the 1D model with an infinite lateral extent. Therefore, caution should be taken when applying one-dimensional interpretation results to 3D geological targets, as significant interpretation errors may occur.

Figure 9 shows the total EMF, full-time apparent resistivity, and secondary anomalous response of the 2D and 3D models at 1.02 ms. As shown in Figure 9a,d, the total EMF is distorted by the conductive body, exhibiting a downward shift above the anomaly. The corresponding secondary anomalous responses, shown in Figure 9c,f, clearly delineate the anomalous bodies with more concentrated anomalies. In the full-time apparent resistivity distributions (Figure 9b,e), both the 2D and 3D models exhibit a high-resistivity zone on the source side and a low-resistivity zone on the opposite side. The apparent-resistivity anomaly of the 2D model has a significantly larger amplitude range than that of the 3D model. Furthermore, the secondary anomalous response of the 2D model exhibits an elongated bipolar anomaly along the strike, whereas that of the 3D model is more localized and resembles the apparent-resistivity distribution, indicating that its morphology is mainly controlled by the relative position between the anomalous body and the source.

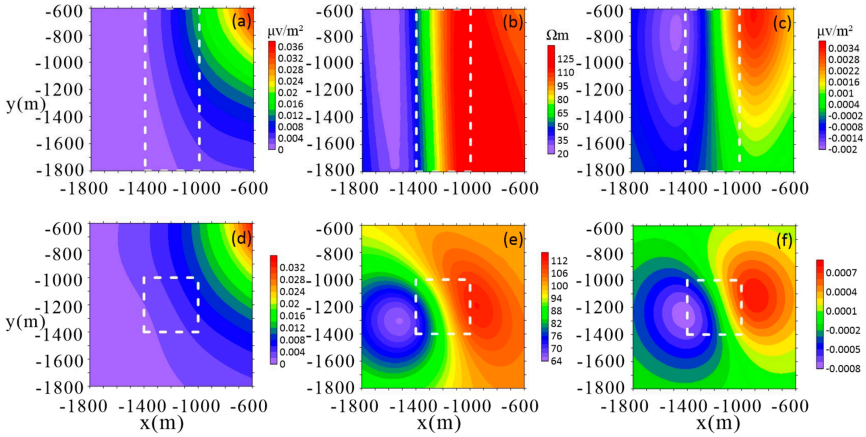


Figure 9. Comparison of dbz/dt, full-time apparent resistivity and secondary anomalous response for the 2D and 3D models at t = 1.02 ms: (**a**–**c**) 2D model, (**d**–**f**) 3D model. Note: The white dotted box indicates the location and range of the abnormal body.

Figure 10 shows the profile map of 2D geological body and 3D geological body center line (y = −1200). It can be found that the anomaly amplitude of 2D object body is much larger than that of 3D object body. According to center line section map, the abnormal response of two-dimensional geological body is quite different from that of three-dimensional geological body in horizontal section map and similar in vertical section map, but different in details. In practical exploration, if two-dimensional model results are used to interpret three-dimensional geological body, it will often lead to certain deviations. Therefore, it is necessary to discuss the forward transient electromagnetic response of three-dimensional geological body. At the same time, we also expect that the SOTEM can increase the abnormal amplitude and improve the signal-to-noise ratio and resolution to a certain extent.

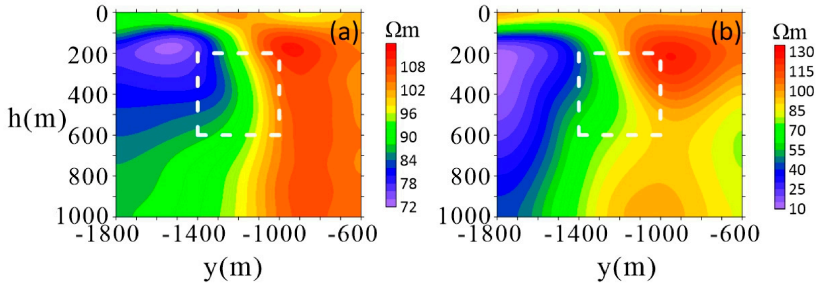


Figure 10. Comparison of full-time apparent resistivity sections for models of different dimensionalities at y = −1200 m: (**a**) 3D model, (**b**) 2D model. Note: The white dotted box indicates the location and range of the abnormal body.

4.3. Characteristic of Abnormal Response for Different Offsets

We still use the above three-dimensional abnormal body model and place the center of the abnormal body at (0 m, −2000 m, 0 m), (0 m, −1200 m, 0 m), (0 m, −800 m, 0 m), respectively, and place the electric source with electric dipole moment of 1000 Am at the origin, as shown in Figure 11. First, we discuss the total EMF, full-time apparent resistivity of the three offset distances at different times, and the distribution characteristics of the secondary field in the measured areas. Figure 12 shows the abnormal response distribution of 2200 m offset at three different times. At 1.02 ms moment, the full-time apparent resistivity appears to have high resistance on one side near the source and low resistance on one side away from the source, as shown in Figure 12b,c, which is similar to Figure 9e,f above, and at this time the abnormal body is in the vertical direction of the source. It can be seen that if the angle between the abnormal body and the source is different, the resulting abnormal response distribution will rotate. With the passage of time, EMF gradually appears as distortion, and the secondary field also appears as sign reversal. This is because in the early times, the current generated by the abnormal body is opposite to the supply current, while in the late stage, with the downward diffusion of the electric field, the direction of the two is the same, resulting in this phenomenon of extreme reversal. In 20 ms, the complete reversal occurs, as shown in Figure 12c,f,i; the abnormal amplitude is also small.

Figures 13 and 14 show the abnormal response distribution of 1200 m offset and 800 m offset, respectively. The abnormal shape is basically the same as the above analysis, but it is worth noting that the abnormal response when the 1200 m offset at 10 ms is similar to the abnormal shape when the 2000 m offset at 20 ms, which indicates that the smaller the offset is, the earlier the time affected by the abnormal body is, as shown in Figures 12g and 13d. This is also verified on the 800 m offset. In addition, with the decrease in offset, the amplitude of secondary field increases, which is beneficial to improve SNR and resolution. This gives the corresponding comparative data later.

Figure 15 shows the EMF of multi-times channel and relative anomaly amplitudes of the center line, respectively. We can see that EMF is enhanced due to the existence of a low-resistance body. For the 2000 m offset, the maximum relative abnormal amplitude is 6% and the relative abnormal amplitude of most time traces is less than 5%, which is not conducive to the recognition of abnormal bodies, as shown in Figure 15a,b. When the offset is reduced, we find that the relative anomaly amplitude is increasing. At the 1200 m offset, the anomaly amplitude reaches about 14%, as shown in Figure 15d. At the 800 m offset, the abnormal amplitude is significantly increased, reaching about 25%, and the multi-times EMF curves shows significant amplitude bending, as shown in Figure 15e,f. This greatly improves the resolution of detecting abnormal bodies. We can also find that the magnitude of total EMF increases with the decrease in offset, which is significant to improve the signal-to-noise ratio and the ability of anti-interference.

Figure 16 shows the profiles of vertical and horizontal central lines of three different offsets. Figure 16a–c shows the central line parallel to the source. At this time, there is a low resistivity trap. With the decrease in offsets, the abnormal amplitude increases and the resolution of low resistivity body increases. Figure 16d–f shows the profile perpendicular to the source, and the abnormal amplitude also increases with the decrease in offset. The high-resistance response appears on the side close to the source, and the low-resistance response appears on the side far away from the source, which corresponds to the slice chart above. In addition, we find that the low-resistance morphology appears in a shallow depth (i.e., the occurrence time is earlier), while the high-resistance characteristics appear later. Therefore, in the early stage, the phenomenon of low-resistance characteristic is more obvious than that of high resistance, which corresponds to the previous slice map, such as Figures 12b, 13b and 14b.

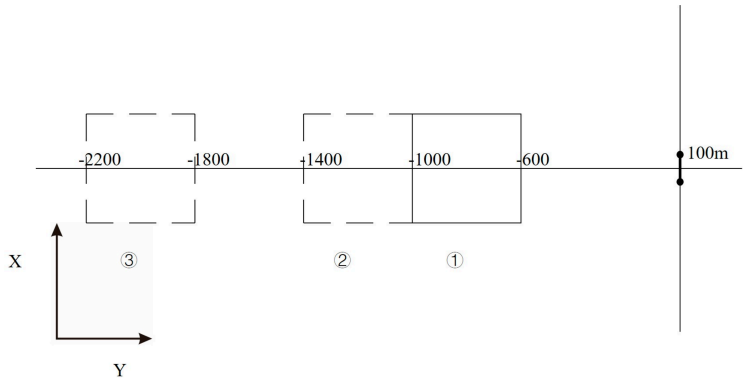


Figure 11. Model configurations with different y-direction offsets between the anomaly-body center and the source: ① 800 m, ② 1200 m, ③ 2000 m.

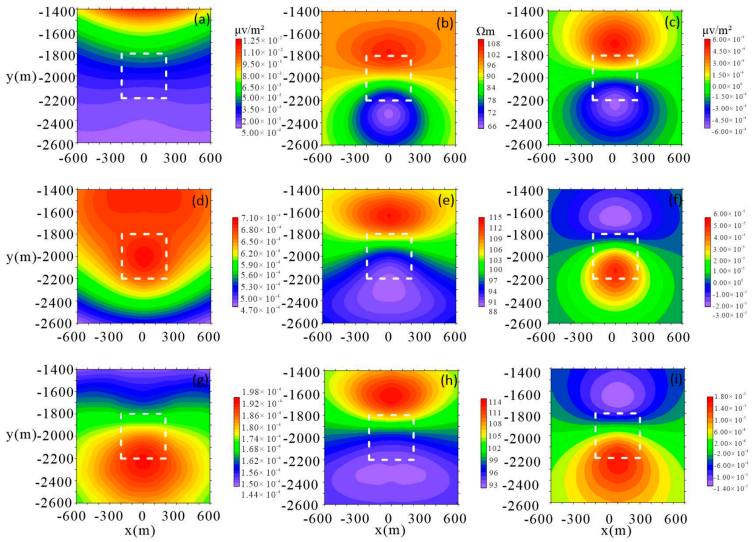


Figure 12. Comparison of db/dt, full-time apparent resistivity and secondary anomalous response at different time instants for the model with a 2000 m offset: (**a**–**c**) 1.02 ms; (**d**–**f**) 10 ms; (**g**–**i**) 20 ms. Note: The white dotted box indicates the location and range of the abnormal body.

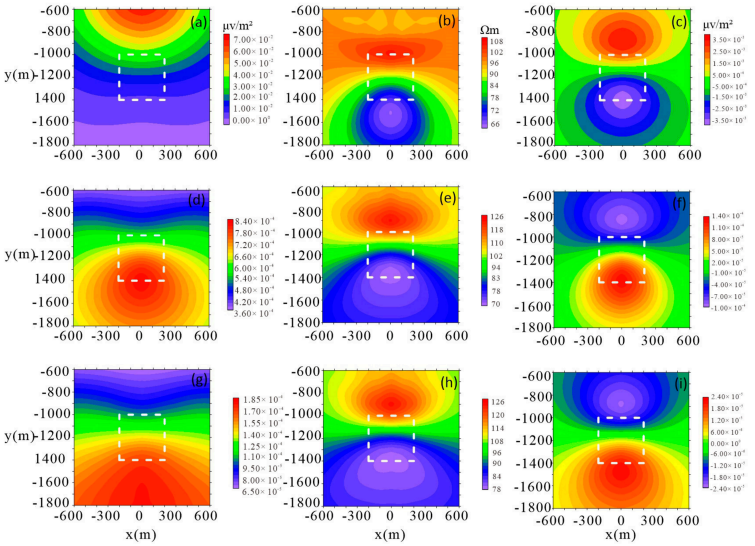


Figure 13. Comparison of db/dt, full-time apparent resistivity and secondary anomalous response at different time instants for the model with a 1200 m offset: (**a**–**c**) 1.02 ms, (**d**–**f**) 10 ms, (**g**–**i**) 20 ms. Note: The white dotted box indicates the location and range of the abnormal body.

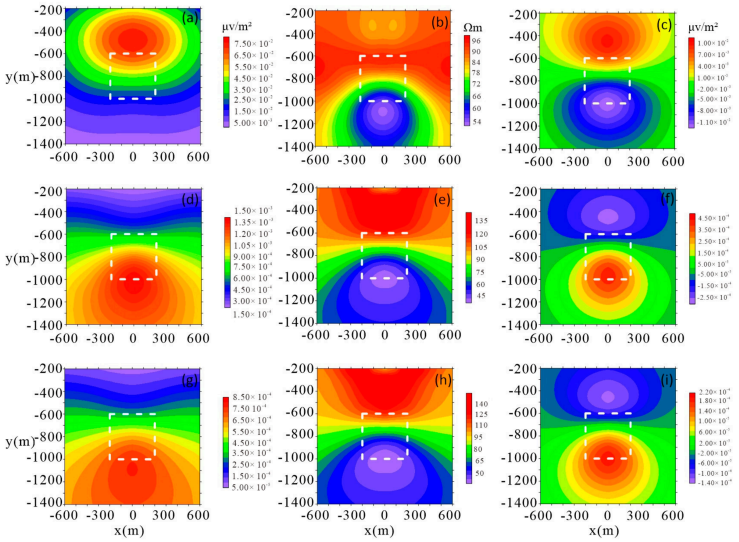


Figure 14. Comparison of db/dt, full-time apparent resistivity and secondary anomalous response at different time instants for the model with a 800 m offset: (**a**–**c**) 1.02 ms, (**d**–**f**) 7.93 ms, (**g**–**i**) 10 ms. Note: The white dotted box indicates the location and range of the abnormal body.

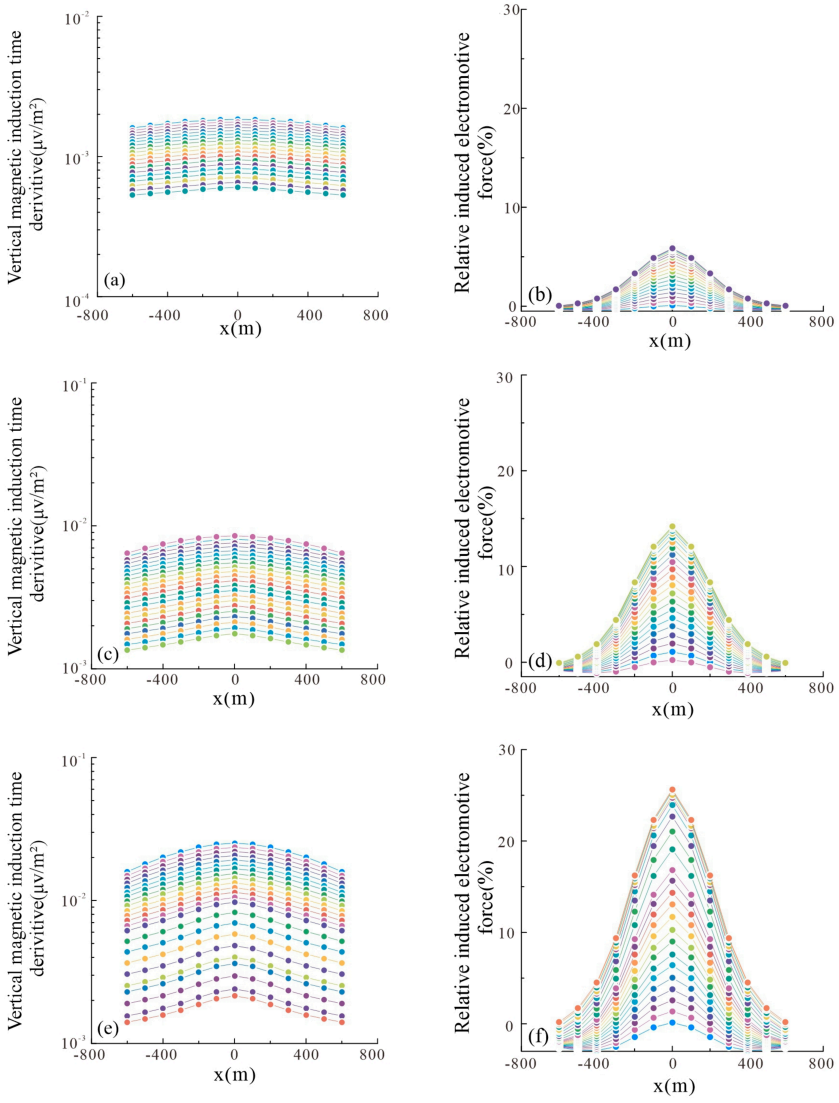


Figure 15. Multi-times channel and relative anomaly magnitude for different offsets: (**a**,**b**) 2000 m offset, (**c**,**d**) 1200 m offset, (**e**,**f**) 800 m offset.

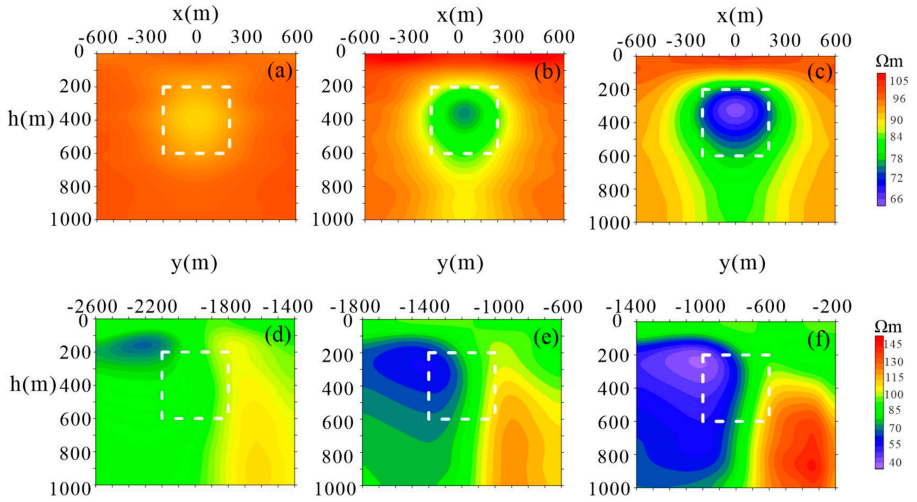


Figure 16. The central full-time apparent resistivity section for different offsets: (**a**,**d**) 2000 m offset, (**b**,**e**) 1200 m offset, (**c**,**f**) 800 m offset. Note: The white dotted box indicates the location and range of the abnormal body.

4.4. Porphyry Copper-Molybdenum Deposit Model

Porphyry copper and porphyry molybdenum deposits represent the most important sources of Cu-Mo resources worldwide. In particular, porphyry molybdenum deposits constitute the dominant type of molybdenum mineralization, with more than 90% of molybdenum deposits being genetically associated with porphyry systems. The contact zone near the top of the porphyry intrusion is generally regarded as the center of mineralization. Figure 17 shows the geological prediction model of the porphyry copper-molybdenum deposit considered in this study. The surrounding rocks of the ore body mainly consist of sedimentary rocks and carbonate rocks. The ore body is located in the shallow part of the deposit and exhibits an approximately circular geometry. Its lateral extension is about 290 m in the x-direction, ranging from x = −145 m to x = 145 m, and about 290 m in the y-direction, ranging from y = −145 m to y = 145 m. In the vertical direction, the ore body extends for approximately 260 m, from z = −483 m to z = −223 m.

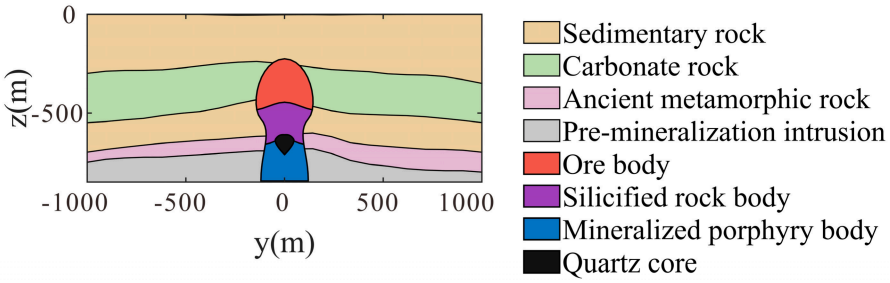


Figure 17. Geological model of the porphyry copper-molybdenum deposit.

The background resistivity of the host earth was set to 1000 Ω·m. The resistivity values assigned to the different geological units in the deposit model are listed in Table 2. For the inclined interfaces of the ore body, a local mesh refinement strategy was adopted to improve the representation of the dipping geological boundaries. Specifically, smaller rectangular hexahedral elements were generated near the ore-body surface, allowing the inclined interfaces to be approximated more accurately by the finite-element grid. Away from the interfaces, relatively larger elements were used to reduce the computational cost while maintaining sufficient accuracy. This hierarchical mesh design provides a balance between geological structure representation and numerical efficiency.

Table 2. Resistivity distribution of the porphyry copper-molybdenum deposit model.

Geological Unit	Resistivity (Ω·m)	Geological Unit	Resistivity (Ω·m)
Sedimentary rock	1500	Carbonate rock	2000
Ore body	1	Ancient metamorphic rock	2800
Breccia	3500	Mineralized porphyry body	800
Pre-mineralization intrusion	900	Silicified rock body	2500
Quartz core	3000		

A 1000 m grounded wire source was deployed on the ground surface, parallel to the y-axis. The two endpoints of the transmitter were located at (1000 m, −500 m, 0 m) and (1000 m, 500 m, 0 m), respectively. Five survey lines were arranged above the ore body along the x-direction. The x-coordinates of the five survey lines were −200 m, −100 m, 0 m, 100 m, and 200 m, respectively. Each survey line was 1000 m long, with receiver positions ranging from y = −500 m to y = 500 m. The receiver spacing was 50 m, and the receiver elevation was 50 m. The survey configuration is shown in Figure 18. The time channels were logarithmically distributed from 10^{-5} s to 10^{-1} s, with a total of 101 sampling times.

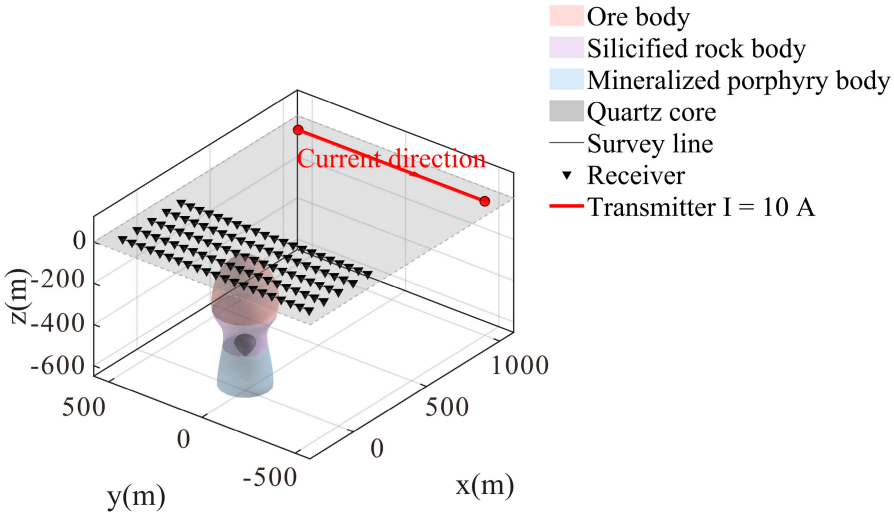


Figure 18. Schematic diagram of the survey configuration.

Figure 19 presents the three-dimensional apparent resistivity imaging result of the porphyry copper-molybdenum deposit model obtained from the short-offset transient electromagnetic forward responses along the five survey lines. The apparent resistivity section was calculated from the simulated response data using the translation algorithm. As shown in Figure 19, a distinct low-resistivity anomaly is clearly observed in the apparent resistivity volume. The lateral extent of the anomaly is mainly concentrated within the range of approximately −150 m to 150 m in both the x- and y-directions, while its vertical distribution is located at depths of approximately 200–500 m. The position, morphology, and burial depth of the low-resistivity anomaly are generally consistent with those of the major mineralized body in the constructed porphyry copper-molybdenum deposit model. This result indicates that the three-dimensional forward response can effectively characterize the spatial distribution of subsurface low-resistivity geological bodies. In addition, a pronounced resistivity contrast can be observed between the anomalous body and the surrounding rocks in the apparent resistivity image. The boundary of the low-resistivity region shows good lateral continuity and is readily identifiable, suggesting that the short-offset transient electromagnetic method has a favorable response to low-resistivity mineralized bodies buried within this depth range. These results further demonstrate the

potential of SOTEM for detecting porphyry-type Cu-Mo mineralization and for delineating the spatial distribution of deep-seated conductive ore-related bodies.

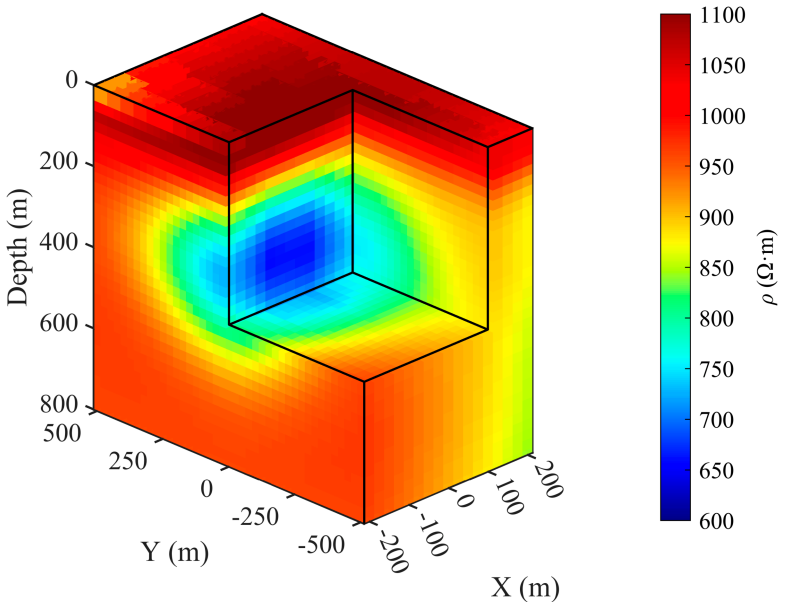


Figure 19. Apparent resistivity imaging result of the porphyry copper-molybdenum deposit model.

5. Conclusions

In this paper, the vector finite element numerical simulation method was used to obtain the electromagnetic response of multi-frequency quickly using the model reduction algorithm, and then the inductive voltage of the SOTEM was obtained using the Fourier inverse transformation. This is a highly efficient numerical modeling method. A translation algorithm was proposed to calculate the full-time apparent resistivity, and through a uniform half-space and a complex 3D model, the correctness of the translation algorithm and vector finite element program were verified. Then we compared the electromagnetic response characteristics of the 1D, 2D, and 3D models, and there were great differences for the abnormal amplitude and the field distribution. In practice, the one-dimensional model forward and inversion theory were used to explain the anomaly generated by the three-dimensional finite geoelectric model, which may result in serious deviations. It is necessary for three-dimensional transient electromagnetic numerical simulation and interpretation. At the same time, we discussed the characteristics of the electromagnetic response and full-time apparent resistivity for different offsets. The porphyry Cu-Mo deposit model experiment further demonstrates that SOTEM three-dimensional forward modeling and full-time apparent resistivity imaging can effectively identify low-resistivity mineralized anomalies buried at depths of approximately 200–500 m, confirming the applicability of this method to realistic mineral deposit model exploration.

Author Contributions: S.Z.: Research design, Method design, Software, Verification algorithm, Experimental research, Writing—original draft. K.C.: Software, Visualization, Writing—original draft. J.Z.: Project management, Funding acquisition, Writing—review & editing. J.L.: Writing—review. X.Y.: Experimental study, Data reduction. All authors have read and agreed to the published version of the manuscript.

Funding: This research was funded by the Special Fund of Deep Earth Probe and Mineral Resources Exploration—National Science and Technology Major Project (No.2025ZD1006201), the Natural Science Foundation of China (NSFC) (U25A202002), the Shaanxi Provincial QinChuangYuan "Scientists + Engineers" Team Project (2025QCY-KXJ-024), and the Open Fund of the State Key Laboratory of Geohazard Prevention and Geoenvironment Protection, Chengdu University of Technology (No.

SKLGP2020K023), for the project "Experimental Study of Semi-Airborne Transient Electromagnetic Exploration for Landslide Geological Survey" (January 2020–December 2022).

Data Availability Statement: The data generated and analyzed during this study are not publicly available due to intellectual property protection and privacy restrictions.

Acknowledgments: The authors give special thanks to a reviewer and the editor for their constructive comments. We are grateful for the financial support from the Special Fund of Deep Earth Probe and Mineral Resources Exploration—National Science and Technology Major Project (No.2025ZD1006201), the Natural Science Foundation of China (NSFC) (U25A202002), the Shaanxi Provincial QinChuangYuan "Scientists + Engineers" Team Project (2025QCY-KXJ-024), and the Open Fund of the State Key Laboratory of Geohazard Prevention and Geoenvironment Protection, Chengdu University of Technology (No. SKLGP2020K023), for the project "Experimental Study of Semi-Airborne Transient Electromagnetic Exploration for Landslide Geological Survey" (January 2020–December 2022).

Conflicts of Interest: The authors declare no conflict of interest.

Appendix A. Complete Derivation of the Variational Functional and the Edge-Element Finite-Element Matrix Equation

This appendix presents the complete derivation from Equation (3) to Equation (4) in the main text and the subsequent discretization of Equation (4) into Equation (6). During the derivation, the finite-element method is used for discretization. The derivation assumes the $e^{i\omega t}$ time convention, neglects displacement currents, treats the electrical conductivity σ as an isotropic scalar, and assumes the magnetic permeability μ to be constant, consistent with the theoretical assumptions adopted in the main text.

Appendix A.1. Application of the Generalized Variational Principle to the Electric-Field Double-Curl Equation

For Equation $\nabla \times \nabla \times \mathbf{E} + k^2\mathbf{E} = -i\omega\mu_0\mathbf{J}_s$, define

$$\begin{cases} \mathrm{L}\mathbf{E} = \nabla \times \nabla \times \mathbf{E} + k^2\mathbf{E} \\ \mathbf{f} = -\mathrm{i}\omega\mu_0\mathbf{J}_s \end{cases} \tag{A1}$$

Substituting these definitions into Equation $F(\Phi) = \frac{1}{2}\langle \chi\Phi, \Phi\rangle - \frac{1}{2}\langle \chi\Phi, u\rangle + \frac{1}{2}\langle \Phi, \chi u\rangle - \langle f, \Phi\rangle$ gives [45]

$$\begin{aligned} \mathrm{F}[\mathbf{E}] &= \frac{1}{2}\int_\Omega \mathbf{E}\cdot\left(\nabla \times \nabla \times \mathbf{E} + k^2\mathbf{E}\right)\mathrm{dV} + \mathrm{i}\omega\mu\int_\Omega \mathbf{E}\cdot\mathbf{J}_s\mathrm{dV} \\ &= \frac{1}{2}\int_\Omega \mathbf{E}\cdot(\nabla \times \nabla \times \mathbf{E})\mathrm{dV} + \frac{1}{2}\int_\Omega \mathrm{k}^2\mathbf{E}\cdot\mathbf{E}\mathrm{dV} + \mathrm{i}\omega\mu\int_\Omega \mathbf{E}\cdot\mathrm{J}_s\mathrm{dV} \end{aligned} \tag{A2}$$

The double-curl term is reduced in differential order using the vector identity

$$\nabla\cdot[\mathbf{E}\times(\nabla\times\mathbf{E})] = (\nabla\times\mathbf{E})\cdot(\nabla\times\mathbf{E}) - \mathbf{E}\cdot(\nabla\times\nabla\times\mathbf{E}) \tag{A3}$$

After integration over the computational domain Ω and successive application of the divergence theorem and the scalar triple-product identity, one obtains

$$\int_\Omega \mathbf{E}\cdot(\nabla\times\nabla\times\mathbf{E})\mathrm{dV} = \int_\Omega (\nabla\times\mathbf{E})\cdot(\nabla\times\mathbf{E})\mathrm{dV} - \int_\Gamma (\mathbf{n}\times\mathbf{E})\cdot(\nabla\times\mathbf{E})\mathrm{dS} \tag{A4}$$

The artificial truncation boundary is placed sufficiently far from the source and anomalous bodies. On the boundary Γ, the homogeneous Dirichlet boundary condition is imposed, as follows:

$$\int_\Gamma (\mathbf{n}\times\mathbf{E})\cdot(\nabla\times\mathbf{E})\mathrm{dS} = 0 \tag{A5}$$

Accordingly, the boundary integral in Equation (A4) vanishes, and the generalized functional becomes [26,45]

$$F[\mathbf{E}] = \frac{1}{2}\int_{\Omega}\Big((\nabla \times \mathbf{E}) \cdot (\nabla \times \mathbf{E}) + k^2\mathbf{E} \cdot \mathbf{E}\Big)dV + i\omega\mu\int_{\Omega}\mathbf{E} \cdot \mathbf{J}_s dV \tag{A6}$$

Equation (A6) is identical to Equation (3) in the main text.

Appendix A.2. Stationarity Condition and Weak Form

Let the electric field undergo an arbitrary admissible variation satisfying the boundary conditions, as follows:

$$\mathbf{E}_\varepsilon = \mathbf{E} + \varepsilon\delta\mathbf{E} \tag{A7}$$

Taking the first variation of Equation (A7), substituting $k^2 = i\omega\mu\sigma$, and noting that Js is a prescribed current source independent of the unknown electric field, gives

$$\delta F = \int_{\Omega}(\nabla \times \delta\mathbf{E}) \cdot (\nabla \times \mathbf{E})dV + i\omega\int_{\Omega}\mu\sigma\delta\mathbf{E} \cdot \mathbf{E}dV + i\omega\mu\int_{\Omega}\delta\mathbf{E} \cdot J_s dV \tag{A8}$$

The variation of each quadratic term produces two identical contributions, which cancel the prefactor 1/2 in the original functional. Imposing the stationarity condition $\delta F = 0$ and moving the source term to the right-hand side yields the finite-element weak form

$$\int_{\Omega}(\nabla \times \delta\mathbf{E}) \cdot (\nabla \times \mathbf{E})dV + i\omega\int_{\Omega}\mu\sigma\delta\mathbf{E} \cdot \mathbf{E}dV = -i\omega\mu\int_{\Omega}\delta\mathbf{E} \cdot \mathbf{J}_s dV \tag{A9}$$

Appendix A.3. Edge-Element Finite-Element Discretization

The computational domain is partitioned into N_e rectangular hexahedral elements $\Omega = \bigcup_{e=1}^{N_e}\Omega_e$, as follows:

$$\int_{\Omega}(\cdot)dV = \sum_{e=1}^{N_e}\int_{\Omega_e}(\cdot)dV \tag{A10}$$

To distinguish the field components from the vectors of degrees of freedom, define as follows:

$$\mathbf{N}_x^e = \begin{bmatrix} N_{x1}^e \\ N_{x2}^e \\ N_{x3}^e \\ N_{x4}^e \end{bmatrix},\ \mathbf{e}_x^e = \begin{bmatrix} E_{x1}^e \\ E_{x2}^e \\ E_{x3}^e \\ E_{x4}^e \end{bmatrix} \tag{A11}$$

The corresponding quantities $\mathbf{N}_y^e, \mathbf{N}_z^e, \mathbf{e}_y^e, \mathbf{e}_z^e$ are defined analogously. Then $E_x^e = (\mathbf{N}_x^e)^T\mathbf{e}_x^e$
$E_y^e = (\mathbf{N}_y^e)^T\mathbf{e}_y^e$, and Equation (4) in the main text can be written compactly as
$E_z^e = (\mathbf{N}_z^e)^T\mathbf{e}_z^e$

$$\mathbf{E}^e = \mathbf{N}_e\mathbf{E}_e \tag{A12}$$

where $\mathbf{N}_e = \begin{bmatrix} (\mathbf{N}_x^e)^T & 0 & 0 \\ 0 & (\mathbf{N}_y^e)^T & 0 \\ 0 & 0 & (\mathbf{N}_z^e)^T \end{bmatrix}$ and $\mathbf{E}_e = \begin{bmatrix} \mathbf{e}_x^e \\ \mathbf{e}_y^e \\ \mathbf{e}_z^e \end{bmatrix} \in \mathbb{C}^{12}$.

In the Galerkin formulation, the weighting functions are chosen to be identical to the interpolation basis functions. Hence,

$$\begin{cases} \delta\mathbf{E}^e = \mathbf{N}_e\delta\mathbf{E}_e \\ \nabla \times \mathbf{E}^e = \mathbf{B}_e\mathbf{E}_e \\ \nabla \times \delta\mathbf{E}^e = \mathbf{B}_e\delta\mathbf{E}_e \end{cases} \tag{A13}$$

where the element curl matrix is

$$\mathbf{B}_e = \begin{bmatrix} 0 & -\frac{\partial(\mathbf{N}_y^e)^T}{\partial z} & \frac{\partial(\mathbf{N}_z^e)^T}{\partial y} \\ \frac{\partial(\mathbf{N}_x^e)^T}{\partial z} & 0 & -\frac{\partial(\mathbf{N}_z^e)^T}{\partial x} \\ -\frac{\partial(\mathbf{N}_x^e)^T}{\partial y} & \frac{\partial(\mathbf{N}_y^e)^T}{\partial x} & 0 \end{bmatrix} \tag{A14}$$

Appendix A.4. Element Matrices and Discrete Equation

Substituting Equations (A13) and (A14) into the element weak form in Equation (A9), the element curl matrix, conductivity matrix, and source vector are defined, respectively, as

$$\mathbf{C}_e = \int_{\Omega_e} \mathbf{B}_e^T \mathbf{B}_e dV \tag{A15}$$

$$\mathbf{M}_e = \int_{\Omega_e} \mu\sigma \mathbf{N}_e^T \mathbf{N}_e dV \tag{A16}$$

$$\mathbf{b}_e = \mu \int_{\Omega_e} \mathbf{N}_e^T \mathbf{J}_s dV \tag{A17}$$

This gives the element residual equation

$$\delta \mathbf{E}_e^T [(\mathbf{C}_e + i\omega \mathbf{M}_e)\mathbf{E}_e + i\omega \mathbf{b}_e] = 0 \tag{A18}$$

Because $\delta \mathbf{E}_e$ is an arbitrary admissible variation, the quantity in square brackets must vanish. The element finite-element equation is therefore

$$(\mathbf{C}_e + i\omega \mathbf{M}_e)\mathbf{E}_e = -i\omega \mathbf{b}_e \tag{A19}$$

The explicit forms of the matrices in Equation (A19) are given in Equation (5) of the main text.

Appendix A.5. Global Assembly and Its Relation to Equation (5)

Let $\mathbf{A}_e$ denote the signed incidence matrix that maps the local edge degrees of freedom of element e to the global edge degrees of freedom. Then

$$\mathbf{E}_e = \mathbf{A}_e \mathbf{E} \tag{A20}$$

Assembling all element equations according to the global edge numbering gives

$$\sum_{e=1}^{N_e} \mathbf{A}_e^T (\mathbf{C}_e + i\omega \mathbf{M}_e)\mathbf{A}_e \mathbf{E} = -i\omega \sum_{e=1}^{N_e} \mathbf{A}_e^T \mathbf{b}_e \tag{A21}$$

Define the global matrices and source vector as $\mathbf{C} = \sum_{e=1}^{N_e} \mathbf{A}_e^T \mathbf{C}_e \mathbf{A}_e$, $\mathbf{M} = \sum_{e=1}^{N_e} \mathbf{A}_e^T \mathbf{M}_e \mathbf{A}_e$, and $\mathbf{b} = \sum_{e=1}^{N_e} \mathbf{A}_e^T \mathbf{b}_e$. The assembled finite-element equation is

$$(\mathbf{C} + i\omega \mathbf{M})\mathbf{E} = -i\omega \mathbf{b} \tag{A22}$$

Equation (5) in the main text omits the explicit incidence matrix $\mathbf{A}_e$ and represents the global assembly by a summation over all elements, as follows:

$$\sum_e (\mathbf{C}_e + i\omega \mathbf{M}_e)\mathbf{E}_e = \sum_e (-i\omega \mathbf{b}_e) \tag{A23}$$

References

1. Chen, W.-y.; Xue, G.; Muhammad, Y.K.; Gelius, L.; Zhou, N.-n.; Li, H.; Zhong, H.-s. Application of short-offset TEM (SOTEM) technique in mapping water-enriched zones of coal stratum, an example from East China. *Pure Appl. Geophys.* **2015**, *172*, 1643–1651. [CrossRef]
2. Zhou, N.; Xue, G.Q. Short-offset grounded-wire TEM method for efficient detection of mined-out areas in vegetation-covered mountainous coalfields. *Explor. Geophys.* **2017**, *48*, 374–382.
3. Xue, G.; Zhang, L.; Zhou, N.; Chen, W. Developments measurements of TEM sounding in China. *Geol. J.* **2020**, *55*, 1636–1643.
4. Strack, K.M.; Lüschen, E.; Köta, A.W. Long-offset transient electromagnetic (LOTEM) depth soundings applied to crustal studies in the Black Forest and Swabian Alps, Federal Republic of Germany. *Geophysics* **1990**, *55*, 834–842. [CrossRef]
5. Xue, G.; Yan, S.; Chen, W. Exploration technique due to grounded wire source with short-offset. *Chin. J. Nonferrous Met.* **2013**, *23*, 2365–2370.
6. Müller, M.; Hördt, A.; Neubauer, F.M. Internal structure of Mount Merapi, Indonesia, derived from long-offset transient electromagnetic data. *J. Geophys. Res.* **2002**, *107*, 2187. [CrossRef]
7. Xue, G.Q. The development of near-source electromagnetic methods in China. *J. Environ. Eng. Geophys.* **2018**, *23*, 115–124. [CrossRef]
8. Di, Q.Y.; Zhu, R.X.; Xue, G.Q.; Yin, C.C.; Li, X. New development of the electromagnetic (EM) methods for deep exploration. *Chin. J. Geophys.* **2019**, *62*, 2128–2138.
9. Xue, G.Q.; Chen, W.Y.; Wu, X. Review on research of short-offset transient electromagnetic method. *J. China Univ. Min. Technol.* **2020**, *49*, 217–228.
10. Chen, W.; Xue, G.; Khan, M.Y.; Li, H. Using SOTEM method to detect BIF bodies buried under very thick and conductive quaternary sediments, Huoqiu Deposit, China. *Pure Appl. Geophys.* **2017**, *174*, 1013–1023.
11. Xue, G.; Chen, W.; Wu, X.; Yan, S.; Guo, W. A near-source electromagnetic method for deep ore explorations. *Minerals* **2022**, *12*, 1208. [CrossRef]
12. Xue, G.; Wu, X.; Chen, W.; Zhou, N. Grounded-source short offset transient electromagnetic method: Theory and applications in deep mineral exploration. *Sci. China Earth Sci.* **2025**, *68*, 626–638. [CrossRef]
13. Chen, W.-Y.; Xue, G.-Q.; Khan, M.Y. Quasi MT inversion of short-offset transient electromagnetic data. *Pure Appl. Geophys.* **2016**, *173*, 2413–2422. [CrossRef]
14. Chen, W.; Xue, G.; Olatayo, A.L.; Chen, K.; Younis Khan, M.; Chen, W.; Zhang, L.; Chen, W. A comparison of loop time-domain electromagnetic and short-offset transient electromagnetic methods for mapping water-enriched zones—A case history in Shaanxi, China. *Geophysics* **2017**, *82*, B201–B208. [CrossRef]
15. Khan, M.Y.; Xue, G.-Q.; Chen, W.-Y.; Boateng, C.D. Investigation of groundwater in-rush zone using petrophysical logs and short-offset transient electromagnetic (SOTEM) data. *J. Environ. Eng. Geophys.* **2020**, *25*, 433–437. [CrossRef]
16. Xue, G.; Wu, X.; Chen, K.; Lei, K.; Zhao, Y.; Lv, P.; Shi, J. An analysis of the shadow effect for the short-offset transient electromagnetic method. *J. Appl. Geophys.* **2022**, *206*, 104833. [CrossRef]
17. Lei, K.; Shi, J.; Chen, W.; Song, W. Shadow effect and source overprint effect of short-offset transient electromagnetic method. *J. Geophys. Eng.* **2023**, *20*, 439–451. [CrossRef]
18. Zhao, Y.; Wu, X.; Chen, W.; Xue, J.; Shi, J. Three-dimensional inversion for short-offset transient electromagnetic data based on 3D U-Net. *J. Geophys. Eng.* **2024**, *21*, 922–937. [CrossRef]
19. Streich, R. 3D finite-difference frequency-domain modeling of controlled-source electromagnetic data: Direct solution and optimization for high accuracy. *Geophysics* **2009**, *74*, F95–F105. [CrossRef]
20. Zhdanov, M.S.; Lee, S.K.; Yoshioka, K. Integral equation method for 3D modeling of electromagnetic fields in complex structures with inhomogeneous background conductivity. *Geophysics* **2006**, *71*, G333–G345. [CrossRef]
21. Ren, Z.Y.; Chen, C.J.; Tang, J.T. A new integral equation approach for 3D magnetotelluric modeling. *Chin. J. Geophys.* **2017**, *60*, 4506–4515.
22. Tang, J.T.; Zhou, F.; Ren, Z.Y. Three-dimensional forward modeling of the controlled-source electromagnetic problem based on the integral equation method with an unstructured grid. *Chin. J. Geophys.* **2018**, *61*, 1549–1562.
23. Ren, Z.; Kalscheuer, T.; Greenhalgh, S. A goal-oriented adaptive finite-element approach for plane-wave 3-D electromagnetic modelling. *Geophys. J. Int.* **2013**, *194*, 700–718. [CrossRef]
24. Ren, Z.Y.; Kalscheuer, T. A finite-element-based domain-decomposition approach for plane-wave 3D electromagnetic modeling. *Geophysics* **2014**, *79*, E255–E268. [CrossRef]
25. Yin, C.C.; Zhang, B.; Liu, Y.H. A goal-oriented adaptive algorithm for 3D magnetotelluric forward modeling. *Chin. J. Geophys.* **2017**, *60*, 327–336.
26. Zhang, J.-F.; Tang, J.-T.; Yu, Y.; Wang, Y.; Liu, C.-S.; Xiao, X. Three dimensional controlled source electromagnetic numerical simulation based on electric field vector wave equation using finite element method. *Chin. J. Geophys.* **2009**, *52*, 3132–3141.
27. Jin, J.M. *The Finite Element Method in Electromagnetics*; Xi'an Electronic University Press: Xi'an, China, 1998.

28. Weiss, C.J. Project APhiD: A Lorenz-gauged A-phi decomposition for parallelized computation of ultra-broadband electromagnetic induction in a fully heterogeneous Earth. *Comput. Geosci.* **2013**, *58*, 40–52. [CrossRef]
29. Ansari, S.; Farquharson, C.G. 3D finite-element forward modeling of electromagnetic data using vector and scalar potentials and unstructured grids. *Geophysics* **2014**, *79*, E149–E165. [CrossRef]
30. Hu, Y.C.; Li, T.L.; Fan, C.S. Three-dimensional tensor controlled-source electromagnetic modeling based on the vector finite-element method. *Appl. Geophys.* **2015**, *12*, 35–44. [CrossRef]
31. Li, J.H.; Farquharson, C.G.; Hu, X.Y. A vector finite element solver of three-dimensional modelling for a long grounded wire source based on total electric field. *Chin. J. Geophys.* **2016**, *59*, 1521–1534.
32. Cai, X.; Hu, J.; Li, J. Parallelized 3D CSEM modeling using edge-based finite element with total field formulation and unstructured mesh. *Comput. Geosci.* **2017**, *99*, 125–134. [CrossRef]
33. Börner, R.U.; Ernst, O.G.; Güttel, S. Three-dimensional transient electromagnetic modelling using rational Krylov methods. *Geophys. J. Int.* **2015**, *202*, 2025–2043. [CrossRef]
34. Commer, M.; Petrov, P.V.; Newman, G.A. FDTD modelling of induced polarization phenomena in transient electromagnetics. *Geophys. J. Int.* **2017**, *209*, 387–405. [CrossRef]
35. Qiu, C.; Güttel, S.; Ren, X.; Yin, C.; Liu, Y.; Zhang, B.; Egbert, G. A block rational Krylov method for 3-D time-domain marine controlled-source electromagnetic modelling. *Geophys. J. Int.* **2019**, *218*, 100–114. [CrossRef]
36. Rochlitz, R.; Seidel, M.; Börner, R.-U. Evaluation of three approaches for simulating 3-D time-domain electromagnetic data. *Geophys. J. Int.* **2021**, *227*, 1980–1995. [CrossRef]
37. Puzyrev, V.; Cela, J.M. A review of block Krylov subspace methods for multisource electromagnetic modelling. *Geophys. J. Int.* **2015**, *202*, 1241–1252. [CrossRef]
38. Rochlitz, R.; Skibbe, N.; Günther, T. custEM: Customizable finite-element simulation of complex controlled-source electromagnetic data. *Geophysics* **2019**, *84*, F17–F33. [CrossRef]
39. Börner, R.U. Numerical modeling in geo-electromagnetics: Advances and challenges. *Surv. Geophys.* **2010**, *31*, 225–245. [CrossRef]
40. Zhou, J.M.; Liu, W.T.; Liu, H. Research on rational Krylov subspace model-order-reduction algorithm for three-dimensional multi-frequency CSEM modeling. *Chin. J. Geophys.* **2018**, *61*, 2525–2536.
41. Zhang, J.; Liu, J.; Feng, B.; Zheng, Y.a.; Guan, J.; Liu, Z. Three-dimensional magnetotelluric modeling using the finite element model reduction algorithm. *Comput. Geosci.* **2021**, *151*, 104750. [CrossRef]
42. Guan, Q.; Tan, H.; Yu, C. 3D modelling of ground magnetic-source airborne TEM data for anisotropic media based on the rational Krylov method. *Explor. Geophys.* **2024**, *55*, 367–381. [CrossRef]
43. Hou, D.; Xue, G.; Zhou, N.; Chen, W.; Xue, J. Exploration of Deep Magnetite Deposit Under Thick and Conductive Overburden with Ex Component of SOTEM: A Case Study in China. *Pure Appl. Geophys.* **2019**, *176*, 857. [CrossRef]
44. Xue, G.; He, Y.; Chen, W.; Wu, X.; Song, W. 3-D inversion based on the particle swarm optimization-quasi-Newton hybrid algorithm for SOTEM. *IEEE Trans. Geosci. Remote Sens.* **2023**, *61*, 5905811. [CrossRef]
45. Jin, J.-M. *The Finite Element Method in Electromagnetics*; John Wiley & Sons: Hoboken, NJ, USA, 2015.
46. Tang, W.W.; Liu, J.X.; Ye, Y.X. Comparison of 3D controlled-source electromagnetic forward modeling based on the nodal finite element and the edge-based finite element. *Oil Geophys. Prospect.* **2008**, *53*, 617–624.
47. Ralph-Uwe, B.; Ernst, O.G.; Spitzer, K. Fast 3-D simulation of transient electromagnetic fields by model reduction in the frequency domain using Krylov subspace projection. *Geophys. J. Int.* **2008**, *173*, 766–780. [CrossRef]
48. Jiang, Y.L. *Model Reduction Method*; Science Press: Beijing, China, 2010.
49. Ward, S.H.; Hohmann, G.W. Electromagnetic theory for geophysical applications. In *Electromagnetic Methods in Applied Geophysics, Volume 1*; Nabighian, M.N., Ed.; Society of Exploration Geophysicists, University of Utah: Salt Lake City, NT, USA, 1987.
50. He, J.S. Wide field electromagnetic sounding methods. *J. Cent. S. Univ. Sci. Technol.* **2010**, *41*, 1065–1072.
51. Wang, H.J. Time-domain transient electromagnetism all-time apparent resistivity translation algorithm. *Chin. J. Geophys.* **2008**, *51*, 1936–1942.
52. Liu, W.; Farquharson, C.G.; Zhou, J.; Li, X. A rational Krylov subspace method for 3D modeling of grounded electrical-source airborne time-domain electromagnetic data. *J. Geophys. Eng.* **2019**, *16*, 451–462. [CrossRef]
53. Commer, M.; Newman, G. A parallel finite-difference approach for 3D transient electromagnetic modeling with galvanic sources. *Geophysics* **2004**, *69*, 1192–1202. [CrossRef]

Disclaimer/Publisher's Note: The statements, opinions and data contained in all publications are solely those of the individual author(s) and contributor(s) and not of MDPI and/or the editor(s). MDPI and/or the editor(s) disclaim responsibility for any injury to people or property resulting from any ideas, methods, instructions or products referred to in the content.